Computation of Lagrangian coherent structures from experimental fluid trajectory measurements in a mechanically agitated vessel

Li, Kun; Savari, Chiya; Barigou, Mostafa

DOI:
10.1016/j.ces.2022.117598

Document Version
Publisher's PDF, also known as Version of record

Citation for published version (Harvard):
Li, K, Savari, C & Barigou, M 2022, 'Computation of Lagrangian coherent structures from experimental fluid trajectory measurements in a mechanically agitated vessel', *Chemical Engineering Science*, vol. 254, 117598. https://doi.org/10.1016/j.ces.2022.117598

Chemical Engineering Science 254 (2022) 117598

Contents lists available at ScienceDirect

Chemical Engineering Science

journal homepage: www.elsevier.com/locate/ces

Computation of Lagrangian coherent structures from experimental fluid trajectory measurements in a mechanically agitated vessel

Kun Li, Chiya Savari, Mostafa Barigou *

School of Chemical Engineering, University of Birmingham, Edgbaston, Birmingham B15 2TT, UK

HIGHLIGHTS

- Lagrangian coherent structures are computed from 3D particle tracking measurements.
- LCSs characterise the hidden complex topology of turbulent flow in a stirred vessel.
- Results show that LCSs are related to mixer configuration and macroscale mixing.

ARTICLE INFO

Article history:
Received 8 November 2021
Received in revised form 23 February 2022
Accepted 6 March 2022
Available online 10 March 2022

Keywords:
Lagrangian coherent structures
Finite-time Lyapunov Exponent
PEPT
Mixing
Turbulence

ABSTRACT

In mechanically agitated vessels, bulk flow circulation which plays a leading role in macroscale mixing is controlled by hidden Lagrangian coherent structures (LCSs). We use a numerical finite-time Lyapunov exponent (FTLE) approach, for the first time, to resolve such LCSs. Experimental 3D Lagrangian trajectories obtained from a unique positron emission particle tracking (PEPT) technique are used to drive the FTLE model. By computing forward and backward FTLE fields and extracting repelling and attracting FTLE ridges in various azimuthal planes of the flow, a highly complex flow topology is unravelled which varies significantly with azimuthal position. We demonstrate how LCSs organise and quantify the chaotic behaviour of fluid particle paths that underpin mixing through the exchange of fluid between zones of different kinematics. This new Lagrangian approach driven by unique PEPT data is able to unfold some of the complexities of turbulent flow that are beyond the capability of traditional methods.

1. Introduction

Mechanically agitated vessels are widely used in numerous mixing operations. Their prime role includes reduction of fluid inhomogeneity by reducing gradients of concentration or temperature to achieve good heat/mass transfer rates, or ensuring good physical mixing of basic product ingredients. The fluid mechanics of mechanically agitated vessels has been studied and reviewed in numerous papers and books (Paul et al., 2003; Harnby et al., 1997). Their applications range widely from food and pharmaceutical processing through chemicals and consumer goods, to mining, construction, and power generation industries. Despite these large markets, industrial practices and processes are seldom efficient or optimal because of a severe lack of fundamental understanding of such mixing flows. From a fluid mechanics perspective, the flow fields in question have an extremely complex nature and are highly dependent on local flow behaviour. They are influenced by many factors, including the internal vessel geometry (baffles, bottom shapes, etc.), operation of agitators (pumping direction, clearance), phase properties (density, rheology, number of phases), and flow regime (laminar, turbulent, transient), thus, making our understanding of such flows limited. Behind this complexity lies a world of yet unexploited opportunities as many industrial processes are run under certain conditions, not because they are efficient or optimal but only because they are better understood. Therefore, understanding these complexities and the local details of fluid transport will undoubtedly benefit the design of optimal mixing and segregation protocols, representing a big step towards improving current engineering practice.

Effective mixing relies on the combination of three physical processes: bulk fluid circulation, turbulence eddy diffusion and molecular diffusion. Bulk circulation plays a primary role in overall mixing by conveying materials to all regions of the vessel and coupling with the local diffusion processes. It is governed by flow structures generally referred to as stable and unstable manifolds, also called Lagrangian coherent structures (LCSs), which are special material surfaces that have a flow repelling or attracting nature

* Corresponding author.
E-mail address: m.barigou@bham.ac.uk (M. Barigou).

https://doi.org/10.1016/j.ces.2022.117598
0009-2509/

Nomenclature

Symbols

$\boldsymbol{C}$	the right Cauchy-Green strain tensor (-)
C_{imp}	impeller off-bottom clearance (m)
D	impeller diameter (m)
$\boldsymbol{F}$	flow map (-)
H	height of liquid in vessel (m)
N	impeller rotational speed (s^{-1})
Re_{imp}	impeller Reynolds number (-)
t	time coordinate (s)
T	vessel diameter (m)
T_{rev}	impeller revolution time (s)
v_x, v_y, v_z	velocity (m s^{-1})
$\boldsymbol{X}$	particle locations (m)
x, y, z	Cartesian coordinates (m)

Greek Symbols

Δt	integration time for FTLE calculation (s)
λ	eigenvalue of the right Cauchy-Green strain tensor (-)
μ	liquid dynamic viscosity (Pa s)
ρ	liquid density (kg m^{-3})
σ	finite-time Lyapunov exponent (s^{-1})

Abbreviations

aLCS	attracting Lagrangian coherent strcuture
FTLE	finite-time Lyapunov exponent
$FTLE^-$	backward finite-time Lyapunov exponent
$FTLE^+$	forwardd finite-time Lyapunov exponent
LCS	Lagrangian coherent structure
PEPT	positron emission particle tracking
rLCS	repelling Lagrangian coherent strcuture

(Shadden, 2011; Haller, 2015). These structures are material surfaces advected under the flow, and are termed Lagrangian because they are determined by observing fluid trajectories over time rather than from an instantaneous Eulerian field. They are also termed coherent because they have a distinctive stability over neighbouring material surfaces.

Conventional Eulerian methods used for flow structure identification are typically concerned with the spatial structure of quantities derived from the velocity field, pressure field or their gradients (Green et al., 2007). For example, the Q-criterion (Hunt et al., 1988), λ_2 criterion (Jeong et al., 1995), and swirling strength criterion (Zhou et al., 1999) have been widely used to investigate coherent structures in fluid flows, although none has emerged as a definitive tool of choice. However, they are not invariant to time-dependent rotations, i.e., they are not objective (frame-independent) for existing structures (Green et al., 2007). Lagrangian methods, on the other hand, detect flow structures based on the properties of fluid particle trajectories. Their advantage is their objectivity (frame-independent) and insensitivity to any short-term perturbation in the Eulerian velocity field (Olacy et al., 2010). LCS theory was first established by computing finite-time Lyapunov exponent (FTLE) fields and identifying FTLE ridges as LCSs by Haller and Yuan (2000), and was further elaborated and refined by Shadden et al. (2005, 2009). Olacy et al. (2010) demonstrated the calculation of FTLE fields from the discrete imperfect data and showed that LCSs are robust and insensitive to both random noise and spatial–temporal resolution. Having a strong mathematical basis, the LCS approach has helped providing new fundamental insights and precise descriptions of fluid flows in many areas, which has attracted a lot of interest in the last two decades.

In geophysical flows, the concept of LCS was used to characterise the mesoscale mixing capability of the Mediterranean Sea (D'Ovidio et al., 2004), to predict the spread-out of pollution release for reducing the environmental effects of the Florida coastline (Lekien et al., 2005), to investigate particle dynamics in a hurricane (Sapsis et al., 2009), and to understand the atmospheric transport of invasive Fusarium for pest management and disease control (Tallapragada et al., 2011). In biological fluid flows, LCS applications include studying the transport mechanics of blood flow in a carotid bifurcation or downstream through an aortic valve (Shadden et al., 2010; Shadden and Taylor, 2008), understanding cilium generated fluid flow within the airway surface liquid of the lung (Lukens et al., 2010), and identification of a jellyfish feeding capture region and predator–prey interaction (Peng and Dabiri, 2009). However, LCS theory has received much less attention in the analysis of engineering flows, with applications having been limited to understanding the behaviour of gaseous jets and turbulent cavitating flows (Tang et al., 2012), and the characterisation of vortex interaction within arrays of randomly placed cylinders (Ricardo et al., 2016). LCS theory has a great potential in unravelling hidden transport phenomena in engineering flows, and establishing a clear connection between LCS forms and the dynamic state of fluids should enable a more detailed description of such flows.

The basis of FTLE and LCS computation is the driver data (velocity field) generally obtained from analytic solution, simulation or experimental measurements. Ideal analytic flows have been the principal tools for developing LCS theory and demonstrating its potential (Haller, 2001; Shadden, 2005). CFD (Finn et al., 2013) or SPH simulation (Sun et al., 2016) data have also been exploited to detect LCS in simplified flows which can be reliably solved. Velocity fields have been measured via 2D PIV (Ruppert-Felsot J. E. et al., 2005; Raben et al., 2014) and used to drive 2D FTLE calculations in some real flows. In a stirred vessel, however, flow is highly complex and 3D FTLE and LCS computation necessitates 3D velocity driver data. The technique of positron emission particle tracking (PEPT) (Barigou, 2004) which provides 3D flow data with a high accuracy (Pianko-Oprych et al., 2009) offers a real opportunity to apply FTLE theory to such complex flows.

In this study, we use the LCS theory driven by Lagrangian data afforded by the PEPT technique to study, for the first time, the large-scale coherent fluid motion underlying a turbulent flow inside a mechanically agitated vessel. A suite of Lagrangian analysis tools based on FTLE calculations is developed to identify the hidden coherent structures that govern fluid transport within a specific observation time window. The visualised Lagrangian coherent structures are used to outline the topology of the flow, delineating the boundaries of different kinetic regions and flow directions to reveal local fluid transport details that affect mixing and which cannot be discerned by conventional flow measurement or simulation techniques.

2. Experimental

A fully-baffled mixing vessel of standard configuration, having diameter T = 190 mm was filled with water to a height $H = T$, as illustrated in Fig. 1. Mechanical agitation was achieved by a down-pumping 6-blade 45° pitched-turbine of diameter $D = 0.5\ T$ set at an off-bottom clearance $C_{imp} = 0.33\ T$. The impeller speed

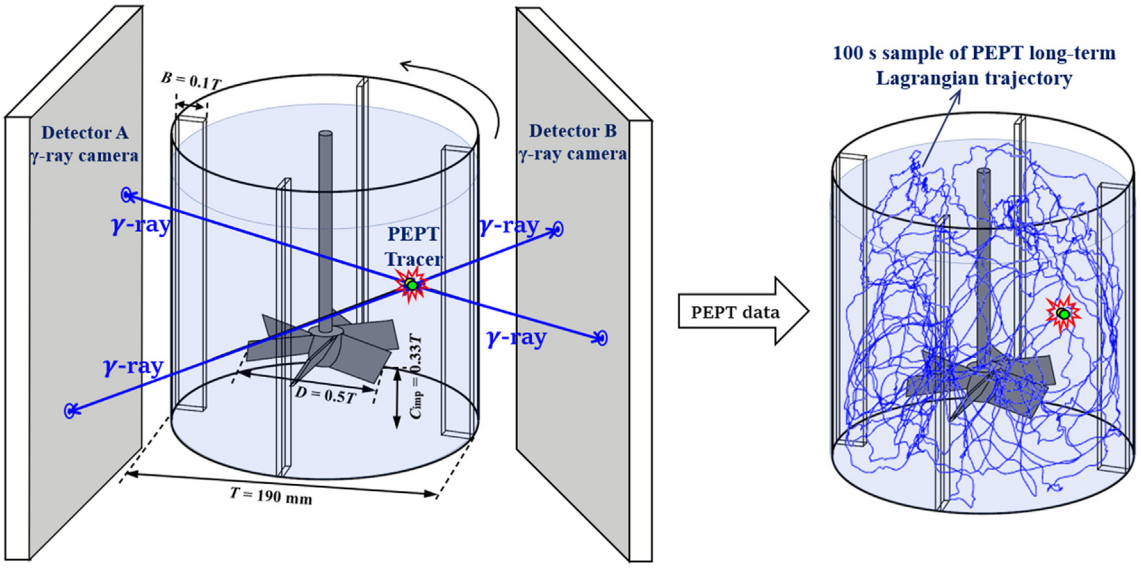

Fig. 1. Setup for PEPT experiment in a mechanically agitated vessel: a tiny neutrally-buoyant particle tracer is tracked in 3D space and time to provide the long-term (6.4 hr) Lagrangian trajectory of water inside the mixing vessel.

was 220 rpm giving an impeller Reynolds number ($Re_{imp} = \rho N D^2/\mu$) of 40,000 which is well within the turbulent regime.

Lagrangian stirred vessel flow measurements were acquired using the PEPT technique in a 6.4 hr experiment. In PEPT, a neutrally-buoyant radio-labelled particle tracer (~100 μm) is injected in the flow and tracked in 3D space and time to determine the long-term trajectory of the fluid (Fig. 1). The technique has an accuracy which is comparable to that of leading optical techniques such as PIV, but with the unique added advantage that it can visualise flow in opaque fluids and inside opaque equipment (Pianko-Oprych et al., 2009). The hardware and software of the technique as well as the associated experimental protocols and raw data analysis procedures have been described in ample detail in our previous work (Barigou, 2004; 2009; Guida et al., 2010a,b; 2012; Eesa et al., 2008; Fangary et al., 2002).

3. Theory

3.1. Eulerian velocity field

The hidden LCSs were extracted from the FTLE fields. The FTLE fields were computed from the Eulerian velocity field available from the PEPT experiment described above. The Lagrangian velocity $\boldsymbol{v}$ was calculated from the time derivative of the trajectory expressed in Cartesian coordinates [x, y, z], thus:

$$\boldsymbol{v} = v_x\boldsymbol{e}_x + v_y\boldsymbol{e}_y + v_z\boldsymbol{e}_z = \frac{\mathrm{d}x}{\mathrm{d}t}\boldsymbol{e}_x + \frac{\mathrm{d}y}{\mathrm{d}t}\boldsymbol{e}_y + \frac{\mathrm{d}z}{\mathrm{d}t}\boldsymbol{e}_z \tag{1}$$

where, t is time and $\boldsymbol{e}_x$, $\boldsymbol{e}_y$ and $\boldsymbol{e}_z$ are unit vectors. The time derivative was calculated using the differencing method, for example, $\frac{\mathrm{d}x}{\mathrm{d}t}$ could be obtained using the ratio of $x_{k+1} - x_k$ to $t_{k+1} - t_k$. Therefore, a new Lagrangian data set [t, x, y, z, v_x, v_y, v_z] was generated. The Eulerian velocity field was constructed from the Lagrangian velocity in each cell using a 3D mesh, as illustrated in Fig. 2. The local velocity in each cell was obtained by calculating the time-average velocity at every detection point within the cell and then averaging by the number of detection points.

3.2. FTLE computation

In chaos theory, the Lyapunov exponent was originally used to measure the growth rate of generic perturbations in a dynamic system, determining the system stability or the sensitivity to its initial conditions. In fluid flow, if two infinitesimally close trajectories separate from an initial small distance $\|\delta\boldsymbol{X}(t_0)\|$ to a further separation $\|\delta\boldsymbol{X}(t)\|$ at some later time, then the separation rate can be expressed by (Shadden et al., 2011):

$$\sigma(\boldsymbol{X}_0, t_0, \Delta t) = \frac{1}{|\Delta t|} \cdot ln\left(\frac{\|\delta\boldsymbol{X}(t)\|}{\|\delta\boldsymbol{X}(t_0)\|}\right) \tag{2}$$

where, σ denotes the finite-time Lyapunov exponent which is a function of time t_0, space $\boldsymbol{X}_0 = (x_0, y_0, z_0)$ and integration time Δt. The ratio $\frac{\|\delta\boldsymbol{X}(t)\|}{\|\delta\boldsymbol{X}(t_0)\|}$ is the expansion coefficient of infinitesimally close trajectories initially starting at two random points. It is worth pointing out that the integration time Δt is generally selected to correspond to the time scale which is appropriate for the description of the flow phenomenon under study.

Let us consider a 3D turbulent flow system whose velocity field is expressed as:

$$\frac{\mathrm{d}\boldsymbol{X}}{\mathrm{d}t} = \boldsymbol{v}(\boldsymbol{X}, t) \tag{3}$$

where, $\boldsymbol{X}(t; \boldsymbol{X}_0, t_0)$, is the trajectory of a fluid particle moving with velocity $\boldsymbol{v}$ from initial position $\boldsymbol{X}_0$ at time t_0 to position $\boldsymbol{X}$ at time t within the flow system. Then the flow map required for the FTLE calculation is defined by: $\boldsymbol{F}_{t_0}^{t}(\boldsymbol{X}_0) \equiv \boldsymbol{X}(t; \boldsymbol{X}_0, t_0)$, consisting of the whole system of trajectories emanating from different initial positions over a given time interval.

Given two arbitrary fluid particles located at positions $\boldsymbol{X}_0$ and $\boldsymbol{X}_0 + \|\delta\boldsymbol{X}(t_0)\|$ at time t_0, their separation distance $\|\delta\boldsymbol{X}(t)\|$ at time t is ideally given by:

$$\|\delta\boldsymbol{X}(t)\| = \boldsymbol{F}_{t_0}^{t}(\boldsymbol{X}_0 + \|\delta\boldsymbol{X}(t_0)\|) - \boldsymbol{F}_{t_0}^{t}(\boldsymbol{X}_0) \tag{4}$$

By expanding the term $\boldsymbol{F}_{t_0}^{t}(\boldsymbol{X}_0 + \|\delta\boldsymbol{X}(t_0)\|)$ in terms of $\|\delta\boldsymbol{X}(t_0)\|$, the separation distance between the two fluid particles can be expressed as:

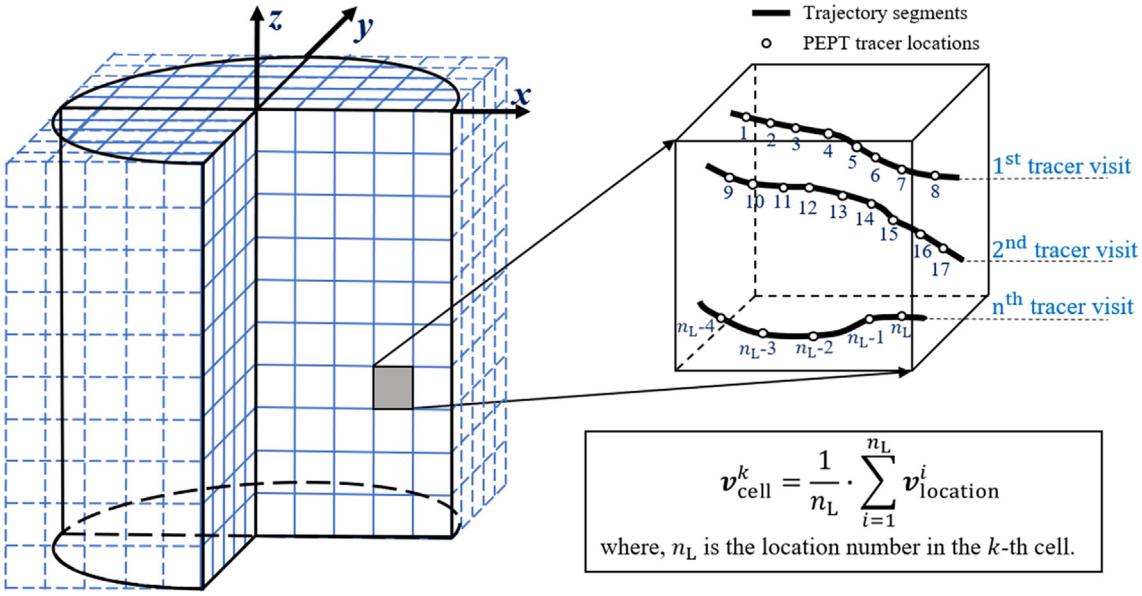

Fig. 2. Illustration of Cartesian grid of equal-volume cubic cells used for analysis of PEPT Lagrangian data - dashed lines show cells outside flow domain: 50 × 50 × 50 cells used for calculation of Eulerian velocity field; 500 × 500 × 500 cells used for computation of FTLE field.

$$\|\delta \boldsymbol{X}(t)\| = \|\nabla \boldsymbol{F}^t_{t_0}(\boldsymbol{X}_0) \cdot \boldsymbol{X}_0\| + O\left(\|\delta \boldsymbol{X}(t_0)\|^2\right) = \sqrt{\boldsymbol{e}^T \cdot \left[\nabla \boldsymbol{F}^t_{t_0}(\boldsymbol{X}_0)\right]^T \left[\nabla \boldsymbol{F}^t_{t_0}(\boldsymbol{X}_0)\right] \cdot \boldsymbol{e}} \cdot \|\delta \boldsymbol{X}(t_0)\| + O\left(\|\delta \boldsymbol{X}(t_0)\|^2\right) \tag{5}$$

where, $\boldsymbol{e}$ is the unit vector in the same direction of the initial separation vector $\delta \boldsymbol{X}(t_0)$, i.e., $\boldsymbol{e} = \frac{\delta \boldsymbol{X}(t_0)}{\|\delta \boldsymbol{X}(t_0)\|}$. Then the expansion coefficient between the two fluid particles over time is:

$$\lim_{\|\delta \boldsymbol{X}(t_0)\| \to 0} \frac{\|\delta \boldsymbol{X}(t)\|}{\|\delta \boldsymbol{X}(t_0)\|} = \sqrt{\boldsymbol{e}^T \cdot \left[\nabla \boldsymbol{F}^t_{t_0}(\boldsymbol{X}_0)\right]^T \left[\nabla \boldsymbol{F}^t_{t_0}(\boldsymbol{X}_0)\right] \cdot \boldsymbol{e}} \tag{6}$$

Letting λ^i be the i-th eigenvalue of the right Cauchy-Green strain tensor:

$$\boldsymbol{C}^t_{t_0}(\boldsymbol{X}_0) = \left[\nabla \boldsymbol{F}^t_{t_0}(\boldsymbol{X}_0)\right]^T \left[\nabla \boldsymbol{F}^t_{t_0}(\boldsymbol{X}_0)\right] \tag{7}$$

With $\boldsymbol{e}^i$ being the i-th eigenvector, the expansion coefficients in the directions of the eigenvectors, i.e., $\delta \boldsymbol{X}(t_0) = \|\delta \boldsymbol{X}(t_0)\| \boldsymbol{e}^i$, are:

$$\lim_{\|\delta \boldsymbol{X}(t_0)\| \to 0} \frac{\|\delta \boldsymbol{X}(t)\|}{\|\delta \boldsymbol{X}(t_0)\|} = \sqrt{\lambda^i} \tag{8}$$

The FTLEs are defined by the ratio of the logarithm of expansion coefficients and the time length $\Delta t = t - t_0$, i.e., the average logarithmic expansion rate:

$$\sigma^i(\boldsymbol{X}_0, t_0, \Delta t) = \frac{1}{|\Delta t|} \cdot \ln\left(\sqrt{\lambda^i}\right) \tag{9}$$

FTLE usually corresponds to the largest value in Equation (9) which measures the expansion rate in the primary expansion direction, and can be expressed as:

$$\sigma(\boldsymbol{X}_0, t_0, \Delta t) = \frac{1}{|\Delta t|} \cdot \ln\left(\sqrt{\lambda_{\max}}\right) \tag{10}$$

where, $\lambda_{\max}$ is the largest eigenvalue of the right Cauchy-Green strain tensor. It should be noted that all initial separation distances $\delta \boldsymbol{X}(t_0)$ have a component in the direction of the $\boldsymbol{e}^i$ vector associated

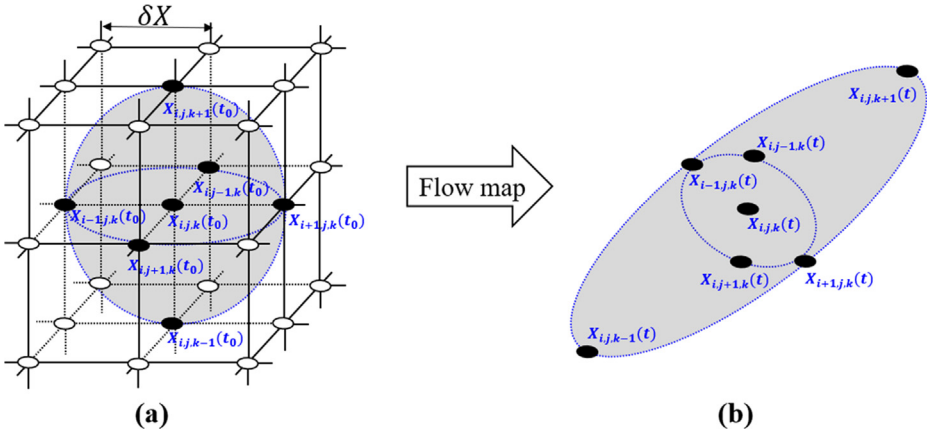

Fig. 3. Illustration of Cartesian grid used to compute the flow map derivative $\nabla \boldsymbol{F}^t_{t_0}(\boldsymbol{X}_0)$ showing example (filled-circle points) for computation at position $\boldsymbol{X}_{i,j,k}(t_0)$: (a) filled-circle points and empty-circle points are initial conditions of all trajectories at initial time t_0; (b) filled-circle points are final positions of trajectories at time t for the flow map derivative at position $\boldsymbol{X}_{i,j,k}(t_0)$.

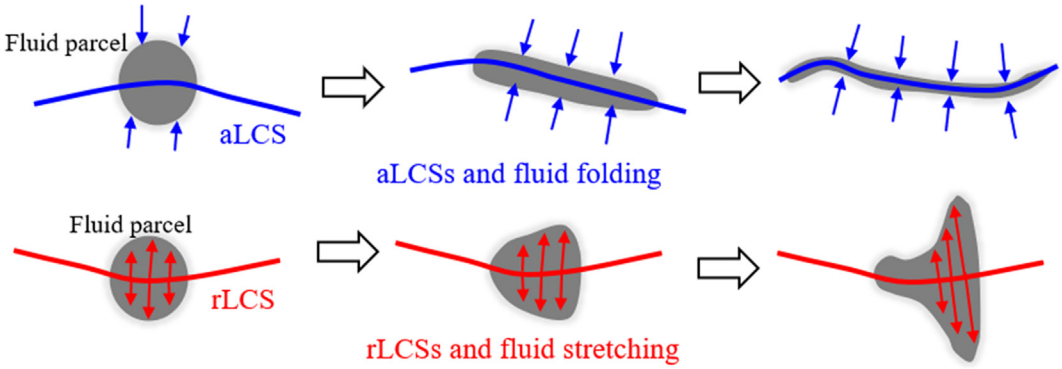

Fig. 4. The role of attracting (aLCS) and repelling (rLCS) LCSs in fluid deformation.

with λ_{max} since the eigenvectors $\boldsymbol{e}^i$ form an orthonormal basis. This means that the growth of the primary component will ultimately dominate the expansion of $\delta\boldsymbol{X}(t_0)$.

To calculate the FTLE in practice, a grid is used which is significantly finer than the grid used to calculate the velocity field, and a passive particle is initialised at each node $\boldsymbol{X}_{i,j,k}(t_0)$ at initial time t_0, as shown in Fig. 3. Such particles are numerically advected to obtain their trajectories by integrating the velocity field, thus:

$$\boldsymbol{X}_{i,j,k}(t) = \boldsymbol{X}_{i,j,k}(t_0) + \int_{t_0}^{t} \boldsymbol{v}(\boldsymbol{X}_{i,j,k}(\tau), \tau) d\tau \tag{11}$$

using the Runge-Kutta integration and velocity spline interpolation schemes for efficient accurate integration. Although a fine grid can sometimes improve the resolution of the FTLE field, too fine a grid may be computationally too expensive; for instance, doubling the FTLE grid density may cause an order of magnitude increase in computation cost. Once the trajectroies are obtained, the flow map derivative $\nabla \boldsymbol{F}_{t_0}^{t}(\boldsymbol{X}_0)$ at each position $\boldsymbol{X}_{i,j,k}(t_0)$ can be calculated by the centre differencing method:

$$\nabla \boldsymbol{F}_{t_0}^{t}\left(\boldsymbol{X}_{i,j,k}(t_0)\right) = \nabla \boldsymbol{F}_{t_0}^{t}\big|_{(x_{i,j,k}(t_0), y_{i,j,k}(t_0), z_{i,j,k}(t_0))}$$
$$\approx \begin{bmatrix} \frac{x_{i+1,j,k}(t)-x_{i-1,j,k}(t)}{x_{i+1,j,k}(t_0)-x_{i-1,j,k}(t_0)} & \frac{x_{i,j+1,k}(t)-x_{i,j-1,k}(t)}{y_{i,j+1,k}(t_0)-y_{i,j-1,k}(t_0)} & \frac{x_{i,j,k+1}(t)-x_{i,j,k-1}(t)}{z_{i,j,k+1}(t_0)-z_{i,j,k-1}(t_0)} \\ \frac{y_{i+1,j,k}(t)-y_{i-1,j,k}(t)}{x_{i+1,j,k}(t_0)-x_{i-1,j,k}(t_0)} & \frac{y_{i,j+1,k}(t)-y_{i,j-1,k}(t)}{y_{i,j+1,k}(t_0)-y_{i,j-1,k}(t_0)} & \frac{y_{i,j,k+1}(t)-y_{i,j,k-1}(t)}{z_{i,j,k+1}(t_0)-z_{i,j,k-1}(t_0)} \\ \frac{z_{i+1,j,k}(t)-z_{i-1,j,k}(t)}{x_{i+1,j,k}(t_0)-x_{i-1,j,k}(t_0)} & \frac{z_{i,j+1,k}(t)-z_{i,j-1,k}(t)}{y_{i,j+1,k}(t_0)-y_{i,j-1,k}(t_0)} & \frac{z_{i,j,k+1}(t)-z_{i,j,k-1}(t)}{z_{i,j,k+1}(t_0)-z_{i,j,k-1}(t_0)} \end{bmatrix} \tag{12}$$

Then the right Cauchy-Green strain tensor given by Equation (7) is computed at each position as a 3×3 matrix, and the corresponding FTLE values are obtained using Equation (10). The FTLE is called forward FTLE ($FTLE^+$) if $\Delta t > 0$ or backward FTLE ($FTLE^-$) if $\Delta t < 0$. $FTLE^+$ and $FTLE^-$ measure, respectively, the rate of separation and attraction between two initially close fluid particles over the time interval $\Delta t = t - t_0$.

3.3. LCS extraction

Once the $FTLE^+$ and $FTLE^-$ fields are computed, it is necessary to locate the LCSs for a clear visualisation of the flow topology. As demonstrated in previous theoretical treatments, FTLE provides an efficient and robust approach to determine the location of flow repelling and flow attracting LCSs which are well-defined by the ridges in $FTLE^+$ and $FTLE^-$ fields, respectively. The direct visualisation of 3D FTLE fields and LCSs is usually impossible. Therefore, visualisation is reduced either to 2D plots or surface triangulation. The former approach is simple and allows depiction of local details on individual 2D sections, while the latter requires a specific ridge extraction algorithm to extract the LCSs (2D materials surfaces) to reveal the hidden flow structures.

A ridge usually refers to a lower-dimensional line or surface that represents the spatial distribution of local maxima, and mathematically it is defined as a curve where the first derivative in its

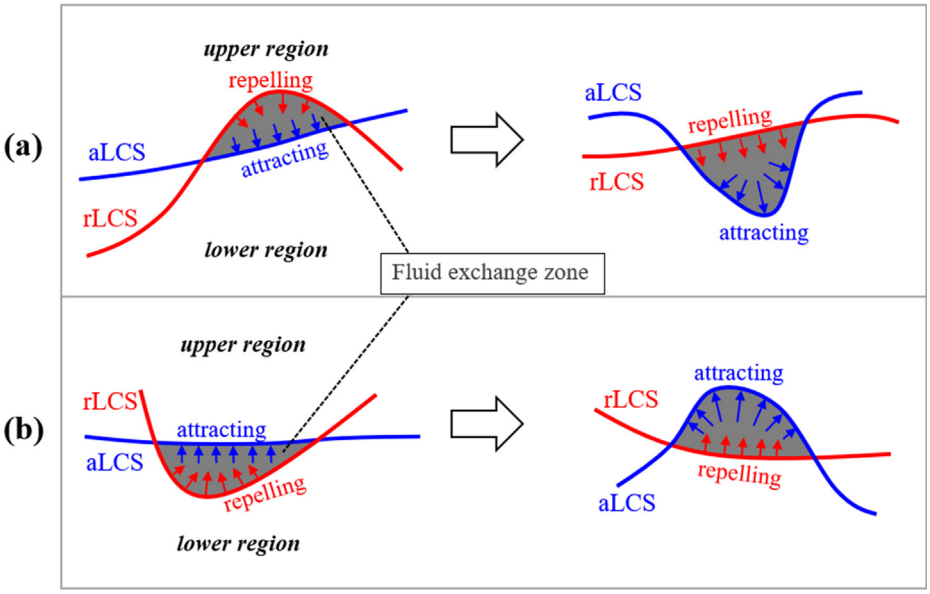

Fig. 5. 2D illustration of possible LCS entanglements and the formation of a fluid exchange zone: (a) aLCS below rLCS; (b) aLCS above rLCS.

normal direction $\boldsymbol{n}$ is zero and its second derivative is negative (Schindler et al., 2011), i.e.,

$$\nabla\sigma \cdot \boldsymbol{n} = 0 \tag{13}$$

$$\langle \boldsymbol{n}, \nabla^2\sigma \cdot \boldsymbol{n}\rangle < 0 \tag{14}$$

Therefore, the extraction of LCS surfaces requires essentially detecting ridges from the FTLE fields, i.e. finding the local maxima of FTLE values through the entire domain and connecting them together to produce a surface. In this study, we extend a 2D grid-based ridge tracking algorithm proposed by Lipinski et al. (2012) to the extraction of 3D ridges. Firstly, the ridge points on the FTLE grid are detected by searching for local FLTE maxima, thus:

$$\sigma(\boldsymbol{X}) \geq \sigma(\boldsymbol{X} \pm \boldsymbol{e}_i), \boldsymbol{e}_i \in \{\boldsymbol{e}_x, \boldsymbol{e}_y, \boldsymbol{e}_z\} \tag{15}$$

where, $\boldsymbol{e}_i$ denotes a vector with a length of grid resolution in coordinate directions. It should be pointed out that the accuracy of the local maxima points, i.e. FTLE ridge points, and, hence, the definition of the ridges is influenced by the resolution of the mesh used. Secondly, a pre-set threshold is applied to filter out the detected ridge points with lower FTLE values so that only the high-value FTLE ridges are delineated. The most useful range for

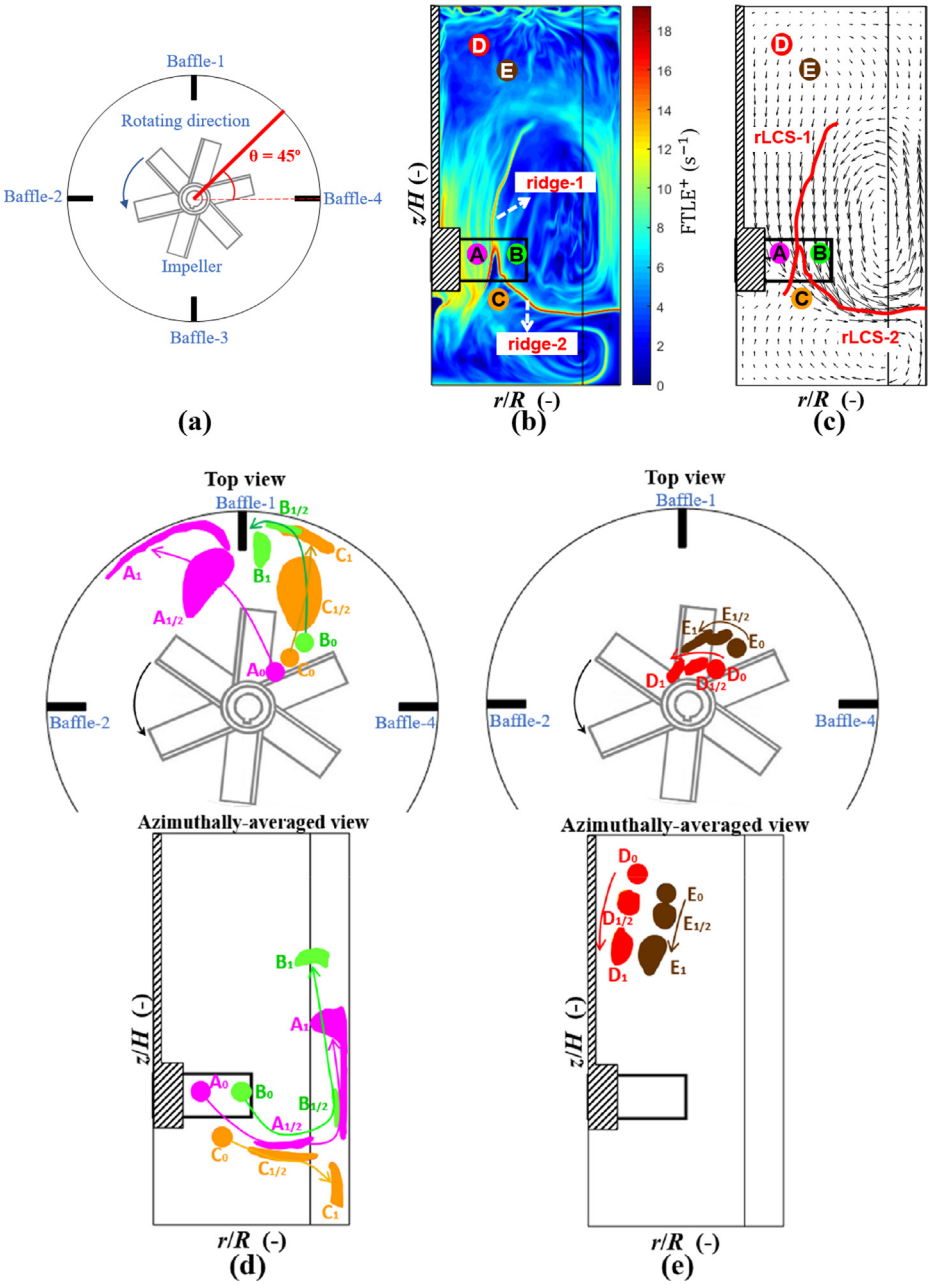

Fig. 6. Identification of (repelling) rLCS in 45° plane and their physical interpretation: (a) 45° plane; (b) FTLE$^+$ map showing local FTLE$^+$ maxima as ridges; (c) extracted (repelling) rLCSs superimposed on velocity vector map; (d) numerically computed future motion during time period T_{rev} of fluid parcels A_0, B_0, C_0 released close to the rLCSs at t = 0, as shown in (c) and (d); (e) numerically computed future motion during time period T_{rev} of fluid parcels D_0, E_0 released far away from the rLCSs at t = 0, as shown in (c) and (e). Subscripts 0, 1/2, 1 correspond, respectively, to time t = 0, +0.5T_{rev} and + T_{rev}.

this threshold is usually 0.75 ∼ 0.9 of the maximum FTLE value, but this may be influenced by the particular application (Shadden et al., 2011). Finally, surface triangulation, which is similar to the marching cube algorithm, is employed to connect the detected ridge points and form LCS surfaces to enable the 3D visualisation of hidden flow structures (Lipinski et al., 2012).

A repelling LCS (rLCS) is associated with $FTLE^{+}$ ridges so that fluid particle trajectories on either side of the ridge diverge away from each other exponentially in forward time, showing the boundaries between different kinetic flow regions. In contrast, an attracting LCS (aLCS) is associated with $FTLE^{-}$ ridges so that fluid particle trajectories on either side of the ridge converge in forward time, delineating the primary flow directions. The repelling and attracting LCSs reveal the hidden flow structures governing fluid transport which are hard to visualise by conventional flow measurement or simulation techniques.

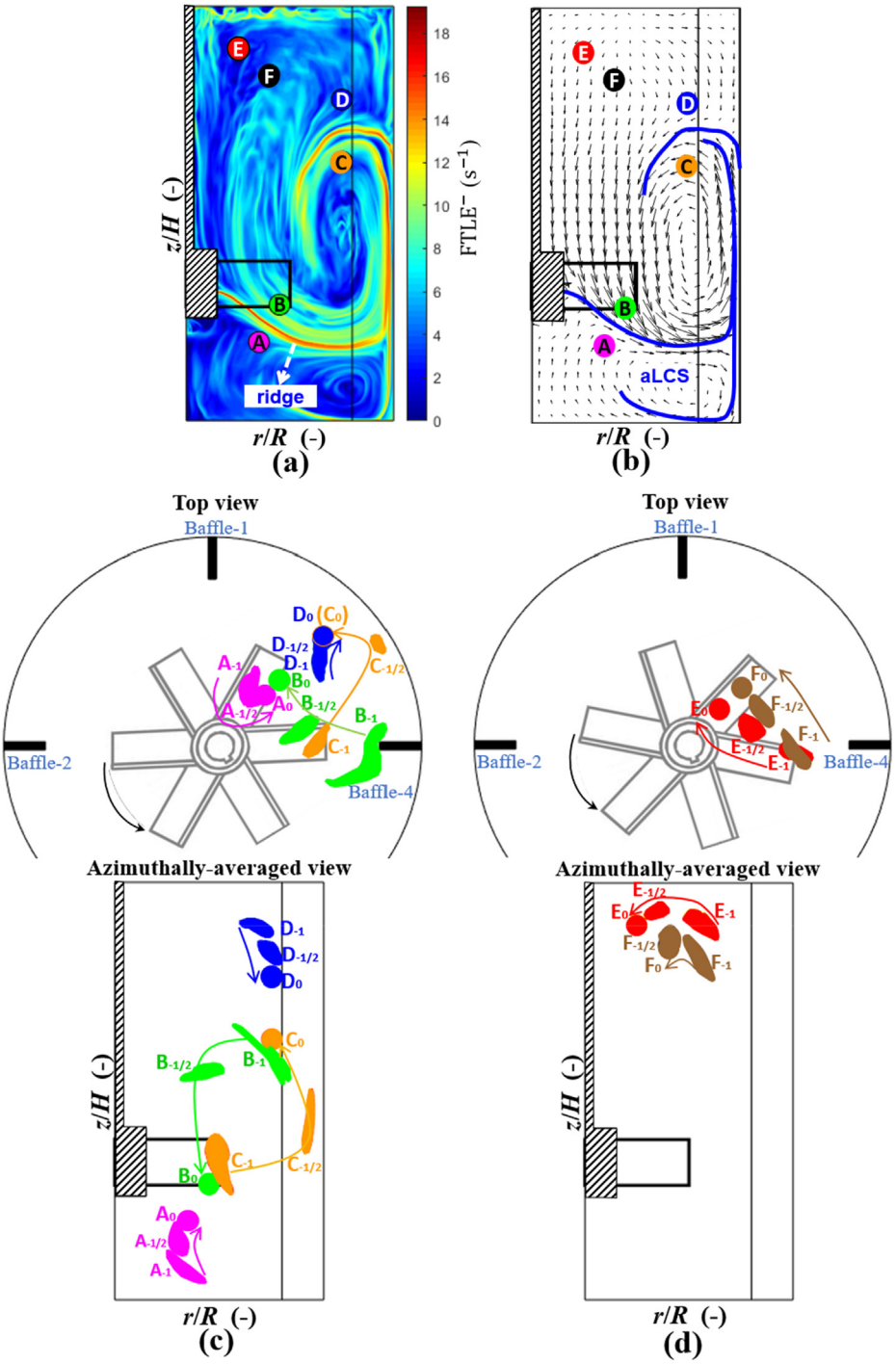

Fig. 7. Identification of (attracting) aLCS in 45° plane and their physical interpretation: (a) $FTLE^{-}$ map showing local $FTLE^{-}$ maxima as ridges; (b) extracted (attracting) aLCSs superimposed on velocity vector map; (c) numerically computed past motion during time period T_{rev} of fluid parcels A_0, B_0, C_0, D_0 released close to the aLCSs at $t = 0$, as shown in (b) and (c); (d) numerically computed past motion during time period T_{rev} of fluid parcels E_0, F_0 released far away from the aLCSs at $t = 0$, as shown in (b) and (d). Subscripts 0, −1/2, −1 correspond, respectively, to past time $t = 0$, $-0.5T_{rev}$ and $-T_{rev}$.

3.4. LCS and fluid transport mechanics

LCSs are special moving flow boundaries which can be used to reveal hidden aspects of fluid transport mechanics. A single repelling or attracting LCS ideally acts as a perfect flow barrier with no fluid transport across it. The local deformation of fluid parcels around an aLCS and rLCS are different, however (Haller and Yuan, 2000). As illustrated in Fig. 4, fluid approaching an rLCS on either side is stretched in the normal direction, so that nearby fluid parcels on either side of the rLCS are repelled in opposite directions resulting in two separated fluid regions with different kinetic behaviour. In other words, rLCS lines (or surfaces/manifolds in 3D) are responsible for local instabilities and flow dispersion. On the other hand, fluid approaching the aLCS on either side undergoes thinning and folding around the line. Thus, the fluid flows alongside the aLCS and adopts its shape, so that the aLCS becomes a primary Lagrangian flow path. An attracting LCS is therefore a cause for local flow stability.

Attracting and repelling LCSs in a given flow tend to occur together which causes their intersection and entanglement. When a pair of aLCS and rLCS are entangled, for example, an enclosed zone is created and the flow is separated into two regions, denoted upper and lower regions in Fig. 5. Inside the enclosed zone, flow is simultaneously repelled by the rLCS and attracted by the aLCS, so that when the rLCS is above the aLCS, it causes the entire zone to gradually flip downwards to reach a stable position, as illustrated in Fig. 5a. In contrast, when the aLCS is above the rLCS the entire zone gradually flips upwards, as illustrated in Fig. 5b. LCS entanglement is a dynamic process and, hence, the fluid inside the enclosed zone will leak out when local disentanglement occurs (Rom-Kedar and Wiggins, 1990), and mixes with other surrounding fluid. The enclosed zone can therefore be considered a fluid exchange zone between the separated regions. The fluid exchange rate and, hence, mixing is proportional to the size of the fluid exchange zone. As an extreme case, two completely overlapped aLCS and rLCS offer a strong barrier to fluid exchange which isolates flow regions and prevents local fluid mixing. Identifying these special dynamic boundaries and their intersection areas can provide valuable information on the mixing performance of a flow system. It is worth noting that based on FTLE calculations, the unravelled coherent structures are computed over a finite time interval, Δt, and because of their dynamic nature they are only valid over such a time interval.

4. Results and discussion

Using the methodology described above driven by long-term PEPT flow trajectory data, a suite of Lagrangian analysis tools based on FTLE calculations were developed to visualise the hidden flow structures in the turbulent flow inside stirred vessels. As pointed out above, the PEPT technique has an accuracy comparable to that of leading optical techniques such as PIV (Pianko-Oprych et al., 2009). The Eulerian velocity field was extracted from the PEPT Lagrangian flow data, as described above, using a Cartesian grid of 50 × 50 × 50 equal-volume cubic cells, as illustrated in Fig. 2. A similar but much finer grid of 500 × 500 × 500 equal-volume cells was used to compute the FTLE field, where the conventional linear interpolation scheme was applied to solve the velocity data at each grid node. One of the important parameters in FTLE calculations is the integration time which is usually selected to be a characteristic time of the flow system at hand (Dauch et al., 2019; Robinso and Cleary, 2011). Here, the integration time used for the main FTLE$^+$ and FTLE$^-$ calculations, T_{rev} = 0.27 s, was equivalent to one impeller revolution which is a characteristic time

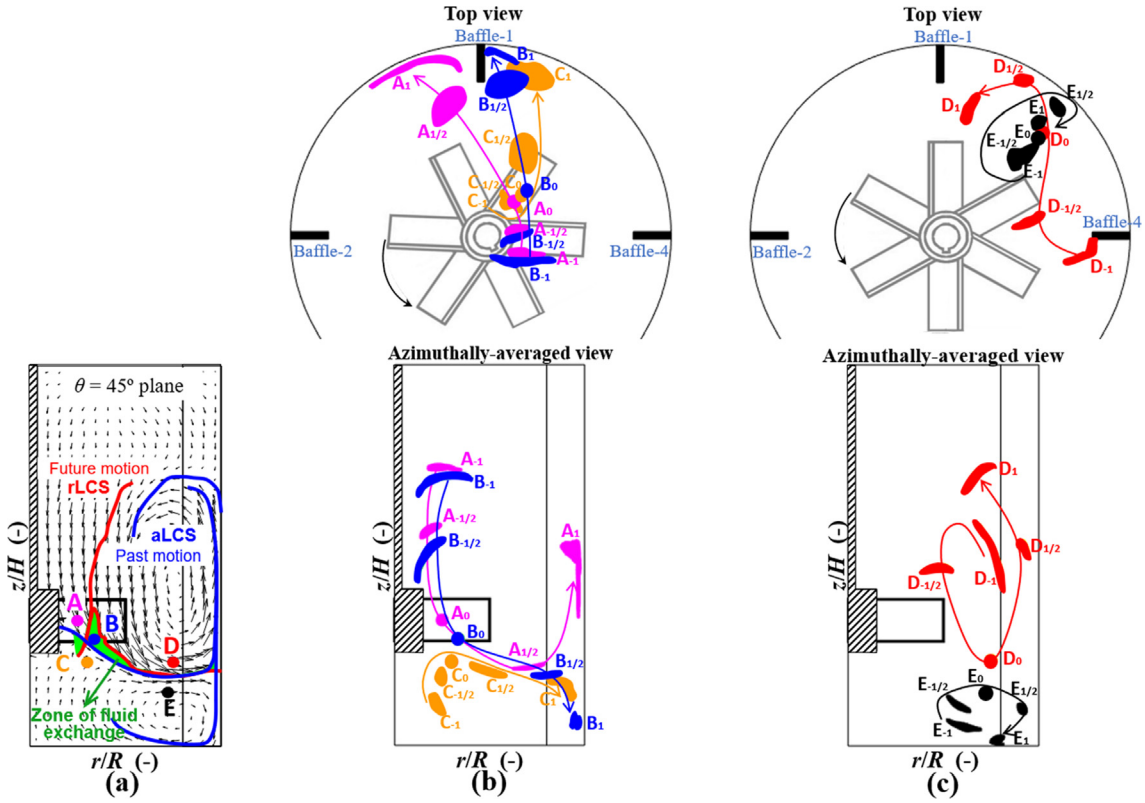

Fig. 8. Interaction of co-existing rLCSs and aLCSs and its effects on flow in the 45° plane: (a) co-existing rLCS and aLCS; (b) numerically computed past and future motion during time period $-T_{rev}$ to $+T_{rev}$ of fluid parcels A_0, B_0, C_0 released at t = 0, as shown in (a); numerically computed past and future motion during time period $-T_{rev}$ to $+T_{rev}$ of fluid parcels D_0, E_0 released at t = 0, as shown in (a).

of the mixing system being studied. The effects of varying the integration time are subsequently explored.

4.1. FTLE maps, LCSs and fluid motion in the 45° plane

Results are presented and discussed in the form of 2D contour plots on different azimuthal planes, giving a detailed description of the flow topology. In this section, we shall first consider the flow in the 45° plane, halfway between two adjacent baffles, as shown in Fig. 6a. The FTLE$^+$ map is presented in Fig. 6b where the local maxima delineate two ridges representing the extracted rLCSs. These rLCSs are made more clearly apparent in Fig. 6c where they are superimposed on the velocity vector map. The pumping action of the impeller creates two flow loops, an anticlockwise loop in the upper part of the vessel and a clockwise loop in the lower part of the vessel below the impeller plane.

4.1.1. Forward FTLE and rLCS

The forward FTLE or FTLE$^+$ measures the rate of separation between two initially close fluid particles over the integration time period ($\Delta t > 0$) and represents the future dynamics of the flow. An illustration of the future motion of fluid parcels released in the 45° plane is depicted to unravel the physical influence of rLCSs on the fluid motion (Fig. 6d, e). Thus, a group of fluid parcels (A, B, C) were numerically introduced on either side of and close to the rLCSs, as shown in Fig. 6c. Each fluid parcel consisted of 10^4 uniformly-distributed fluid particles within the given volume of the parcel. The future 3D individual motion of these particles was numerically tracked by integrating the 3D velocity field over one impeller revolution period (T_{rev}). Thus, as well as the position of the fluid parcels their shape is also obtained. At time $t = 0$, the fluid parcels are at their initial position and are denoted by (A_0, B_0, C_0). Their future shape and position are shown in Fig. 6d at $t = +0.5T_{rev}$ and $+T_{rev}$, corresponding to half a revolution and one full revolution of impeller rotation and denoted, respectively, by ($A_{1/2}$, $B_{1/2}$, $C_{1/2}$) and (A_1, B_1, C_1).

Repelling LCSs are hidden virtual flow barriers produced by the mixing system, which govern future fluid motion. Fluid parcel A_0 which is situated to the left of rLCS-1 moves azimuthally to the leeward side of baffle-1, while being subjected to considerable stretching in the direction of impeller rotation ($A_{1/2}$, A_1). Fluid parcles B_0 and C_0 which are to the right of rLCS-1, however, move to the windward side of baffle-1 while incurring similar but less pronounced deformation ($B_{1/2}$, C_1) than A. On impact with baffle-1, B_1 contracts significantly. It appears that rLCS-1 results from the flow separation effects of baffle-1 between windward and leeward flows. Fluid parcels A_0 and B_0 which are above rLCS-2 do not cross this boundary and remain in the upper flow region. Fluid parcel C_0 which is below rLCS-2 also does not cross this boundary and remains in the lower flow loop. It appears, therefore, that rLCS-2 delineates the boundary between the two main flow loops generated by the impeller.

Whilst fluid parcels (A, B, C) were initially close to the rLCSs, fluid parcels D and E were selected far away from the rLCSs, as shown in Fig. 6c. The rLCSs are loci of maximum FTLE$^+$ values

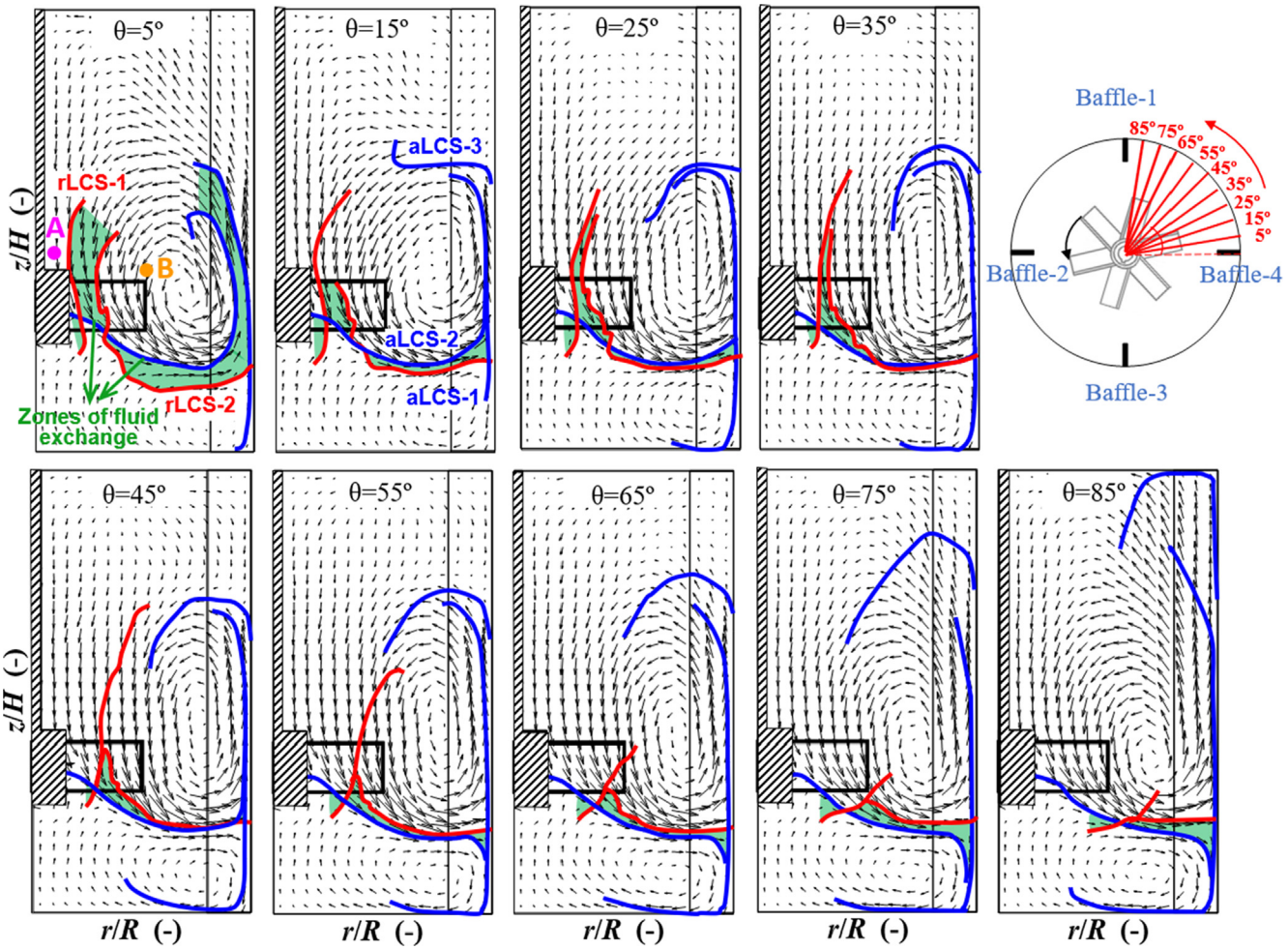

Fig. 9. Effects of azimuthal position on the extracted co-existing LCSs and their interaction.

which separate flow regions of markedly different dynamical behaviours. Their repelling effect is manifested in the deflection of oncoming flow, as demonstrated in the strong deformation and dispersion of fluid parcels (A, B, C). On the other hand, as depicted in Fig. 6e, fluid parcels D_0 and E_0, after a full impeller revolution, move in the same direction incurring a much smaller displacement, smaller deformation and their separation distance is more or less unchanged. Therefore, for example, for mixing processes requiring feeding of materials, the feeding points can be selected near a rLCS to achieve fast distribution of the fed materials in the vessel.

4.1.2. Backward FTLE and aLCS

Having examined the (forward) $FTLE^+$ field inside the mixing vessel, we now discuss the (backward) $FTLE^-$ field which measures the rate of attraction between two initially close fluid particles over the integration time period ($\Delta t < 0$) and represents the past dynamics of the flow. An illustration of the past motion of fluid parcels released in the 45° plane is depicted to unravel the physical influence of aLCSs on the fluid motion (Fig. 7c, d). Thus, a group of fluid parcels (A, B, C, D) were numerically introduced on either side of and close to the aLCSs, as shown in Fig. 7a, b. The computed historical shape and position of these fluid parcels are shown in Fig. 7c at $t = 0$, $-0.5T_{rev}$ and $-T_{rev}$, with positions denoted, respectively, by 0, $-1/2$ and -1.

Similar to repelling LCSs, aLCSs are also hidden virtual flow barriers produced by the mixing system, which influence past fluid motion. Fluid parcels (A, B, C, D) were selected initially close to the aLCSs, whilst fluid parcels E, F were selected far away from the aLCSs, as shown in Fig. 7a, b. The aLCSs are loci of maximum $FTLE^-$ values which separate flow regions of markedly different past dynamical behaviours. Fluid parcel couples (A, B) and (C, D) which are initially close to but on either side of an aLCS are shown to deform differently and originate from very disparate locations, indicating that the flow around an aLCS is diverse. The attracting effect of aLCSs is, thus, manifested in their diverse oncoming flow. Fluid parcels (E, F) which are initially remote from any aLCS but close to each other, are shown to incur similar deformation and have been close to each other all along, indicating that away from the aLCS flow is much less diverse.

4.1.3. Interaction of co-existing rLCSs and aLCSs

In the above, repelling and attracting LCSs were considered in isolation in order to describe their individual effects on the dynamics of the flow. In reality, however, they occur simultaneously and their interaction leads to entanglement, i.e. rLCS and aLCS have intersected points. These LCSs delineate boundaries between regions of different flow dynamics which undergo a certain amount of fluid exchange between them. The interaction and entanglement of co-exiting rLCSs and aLCSs and their effects on flow behaviour are illustrated in Fig. 8. In Fig. 8a the intersection of the rLCSs with the aLCSs creates a common zone of fluid exchange between the different confined regions delineated by the different LCSs. For example, in the past fluid parcel B was located in the flow region above the aLCS, whereas in the future, B is located in the flow region below the rLCS. Thus, over time, B has moved from the upper flow loop down to the lower flow loop, following the pathline depicted in Fig. 8b. This movement applies to all fluid contained in the zone of fluid exchange. In facilitating fluid exchange between the upper and lower flow loops, such a zone promotes fluid mixing. The size of the fluid exchange zone will determine the extent of its contribution to mixing.

Now, considering fluid parcels A and D, because they are located above the rLCS as well as the aLCS, their pathlines remain confined in the upper flow loop and cannot enter the lower flow loop (see Fig. 8b, c). Similarly, fluid parcels C and E being located below the rLCS as well as the aLCS, they are trapped in the lower flow loop and cannot move to the upper flow loop (see Fig. 8b, c).

4.2. Effects of azimuthal position on LCSs and their interaction

The extracted LCSs are depicted in different azimuthal planes over a whole quadrant from 5° to 85°, as shown in Fig. 9. These

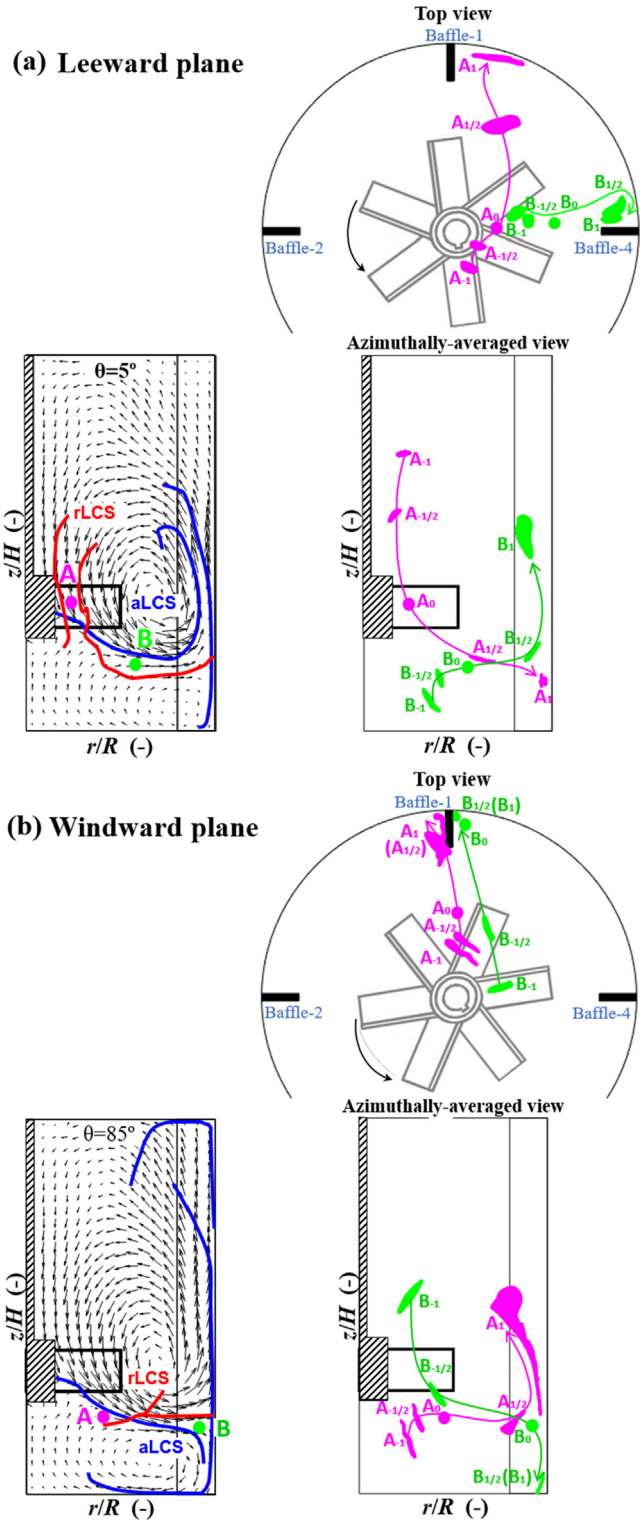

Fig. 10. Interaction of co-existing rLCSs and aLCSs and its effects on zonal fluid exchange in (a) the leeward (5°) plane and (b) the windward (85°) plane.

plots represent in effect the changes in the topology of the LCS surfaces/manifolds. As discussed above, as the impeller rotates anticlockwise, rLCS-1 is a consequence of the separation effects between the windward and leeward flows around baffle-1, whilst rLCS-2 delineates the boundary between the two main flow loops generated by the impeller. Moving from the 5° plane which is the leeward side of a baffle towards the 85° plane, i.e. the windward side of the next baffle, the rLCSs move closer to each other. Beyond the 45° plane, they become gradually shorter while moving towards the wall. The consequence of such topological changes is that, as the azimuthal position increases from 5° onwards, more and more of the fluid to the left of rLCS-1, represented by A in Fig. 9, is driven to the leeward side of baffle-1, whilst less and less fluid from the inner region to the right of rLCS-1, denoted by B, remains confined within the windward side of baffle-1. Hence, the baffling effect reduces with increasing azimuthal position, such that at 85°, baffle-1 has little effect on the swirling fluid motion and most of it passes to the leeward side.

The observed aLCSs separate flow regions of markedly different past dynamical behaviours, in this case the upper and lower flow loops, as depicted in Fig. 8. With increasing azimuthal position from 5° to 85°, the lower aLCS delimiting the bottom flow loop undergoes little change in its topology, whilst the higher aLCSs grow upwards to keep up with the upper flow loop expanding owing to the flow becoming increasingly more axial near the wall on approach to the windward side of baffle-1.

The interaction of the rLCSs and aLCSs creates a zone of fluid exchange, as shown in Fig. 8. Such a zone is relatively large in the 5° plane and seems to surround most of the upper flow loop. Away from this plane, the fluid exchange zone shrinks gradually to reach a minimum at the halfway (45°) plane due to the gradual overlap of the rLCSs and aLCSs and their switch of position relative to each other, before expanding slightly again.

It thus appears that the leeward side of a baffle, i.e. 5° plane, contains the most fluid exchange between the two main flow loops. Such fluid exchange is illustrated in more detail in Fig. 10a. Fluid parcel A which is located below a rLCS originates from the upper part of the vessel and moves towards the bottom. In contrast, B which is located below a aLCS originates from the lower part of the vessel and moves to the upper part of the flow. As pointed out above, with increasing azimuthal position, the order of the rLCS and aLCS lines is gradually reversed and so is the flow exchange, as exemplified by the plots in Fig. 10b corresponding to the windward (85°) plane.

4.3. Effects of integration time on number and topology of LCSs

In the above sections, the LCSs were calculated using an integration time equivalent to one impeller revolution (T_{rev}). As the integration time increases, we may expect more LCSs to emerge revealing further fluid transport phenomena. However, a higher number of LCSs can be hard to analyse as it leads to highly complex structures. To illustrate this situation, we computed the FTLE maps using an integration time equal to $2T_{rev}$, i.e. two impeller revolutions, and sample results are presented in Fig. 11 for the 45° plane.

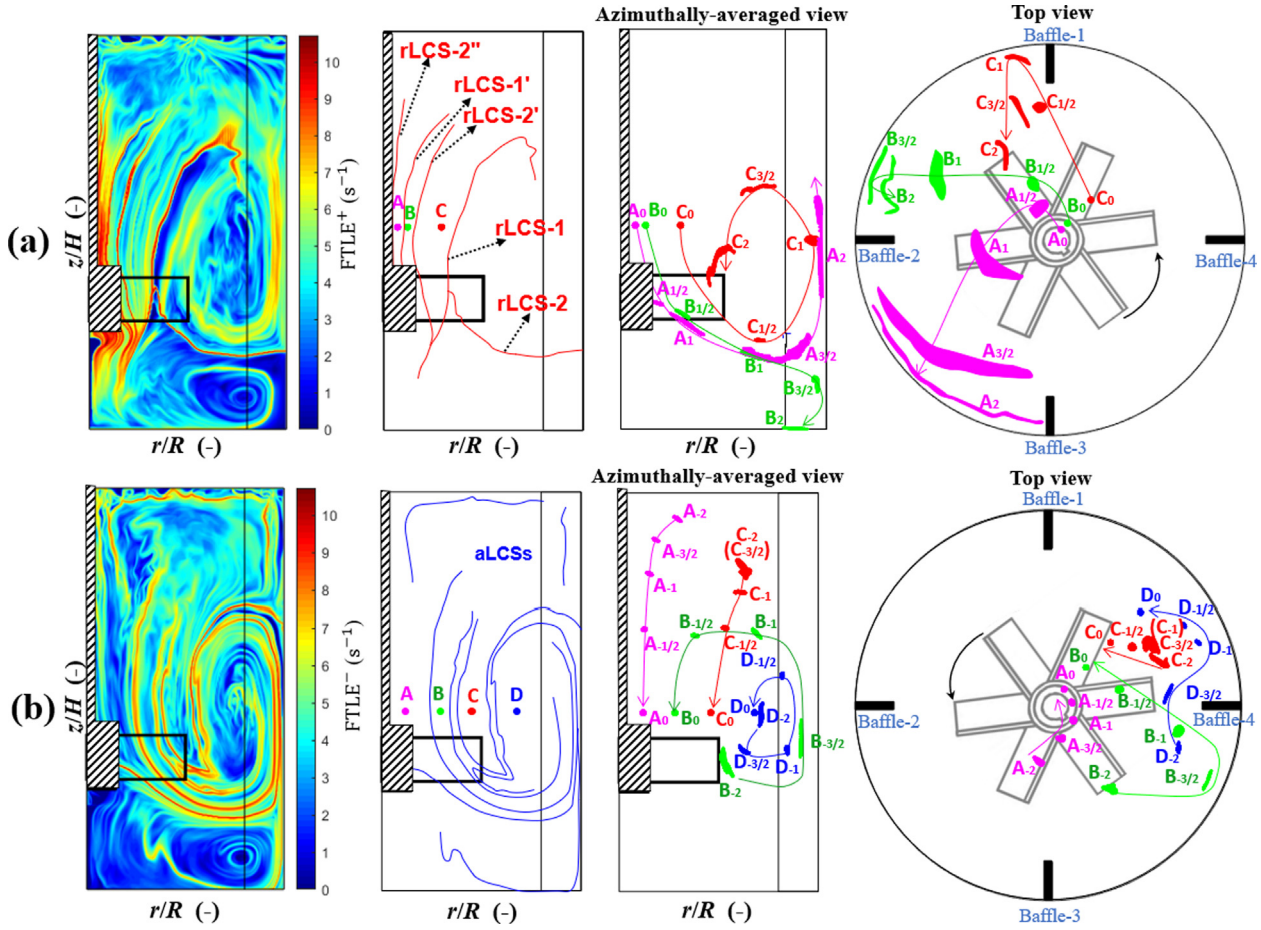

Fig. 11. The effects of doubling the integration time ($2T_{rev}$) on the number and topology of the LCSs observed in the 45° plane: (a) FTLE^{+} map, rLCSs and future fluid motion; (b) FTLE^{-} map, aLCSs and past fluid motion.

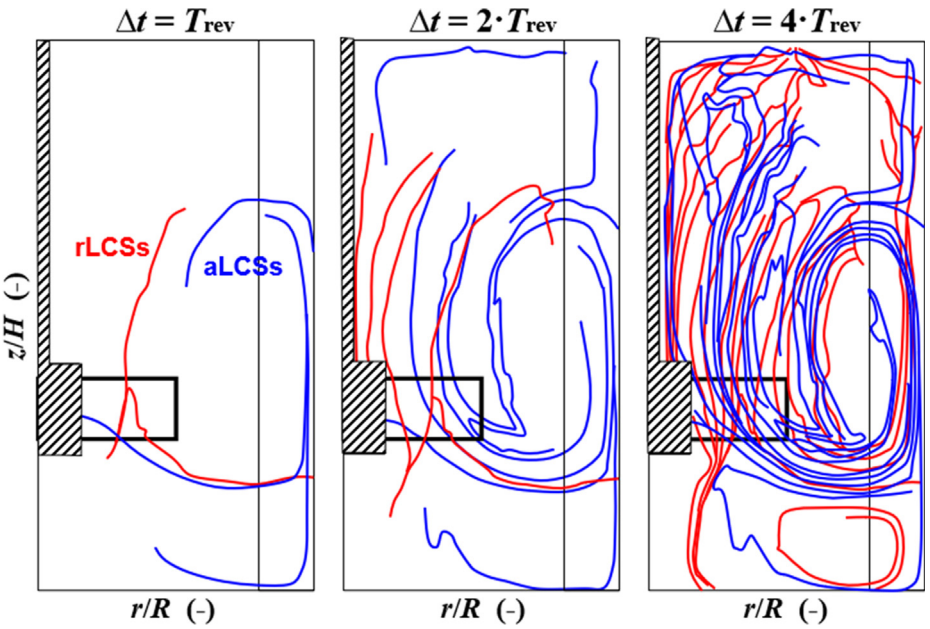

Fig. 12. The effects of integration time on the number and topology of the co-existing rLCSs and aLCSs observed in the 45° plane.

As depicted in Fig. 11a, rLCS-1 and rLCS-2 extracted from the $FTLE^{+}$ field computed in the first impeller revolution are observed again, with rLCS-1 having grown considerably. A new rLCS-1′ analogous to rLCS-1, i.e. resulting from the flow separation effects of baffle-2 between windward and leeward flows, as illustrated by the motion of fluid parcels A and B. Similarly, the additional rLCS-2′ and rLCS-2″ which are newly visualised represent new surfaces/manifolds that also lie at the boundary between the upper and lower flow loops, as demonstrated by the motion of fluid parcels B and C. The $FTLE^{-}$ results plotted in Fig. 11b show an ensemble of new aLCSs, revealing more details of the complexities characterising the history of the fluid motion.

If the integration time is increased further, new rLCSs of type 1 and 2 unravel, as depicted in Fig. 12 where results are displayed for integration times equivalent to T_{rev}, $2T_{rev}$ and $4T_{rev}$. Note that $4T_{rev}$ corresponds to the circulation time in the vessel, i.e. the time measured from when a fluid particle leaves the impeller horizontal mid-plane until it returns to it (Davidson et al., 2003; Guida et al., 2012), which can be considered as another characteristic time of the mixing system. Clearly, a longer integration time uncovers more LCSs and a highly complex flow topology. The large number of LCSs leads to more LCS intersections and more uniformly-distributed LCSs entanglements, thus, enhancing fluid exchange throughout the vessel and achieving better mixing. It becomes clear, therefore, that the level of complexity of the uncovered hidden flow structures is an indication of the quality of fluid mixing. Detailed analysis of such complex flow topologies, however, poses an immense challenge because of the entanglement of the LCSs.

5. Conclusions

A suite of Lagrangian analysis tools has been developed to compute the forward and backward FTLE fields which characterize turbulent fluid mixing in a mechanically agitated vessel. The computations have been driven by experimental long-term Lagrangian trajectory data obtained from a unique positron emission particle tracking technique. Whilst FTLE computations in the literature have generally dealt with simple idealized flows with a smooth velocity field that is known accurately, the FTLE model developed here has contended with the challenges of a 3D discrete experimental velocity field to successfully unveil hidden Lagrangian coherent structures.

The extraction and identification of repelling and attracting FTLE ridges has enabled the unravelling of a highly complex flow topology. Repelling LCSs are responsible for local instabilities and flow dispersion, whereas attracting LCSs lead to local fluid thinning and folding and cause local flow stability. LCSs computed in various vertical planes of the flow have shown that the conventional concept of azimuthally-invariance cannot be assumed in a baffled vessel since flow transport features vary significantly with azimuthal position. The interaction and entanglement of LCSs have been shown to underpin fluid mixing by the creation of zones of fluid exchange between flow regions of different kinematics. A large number of LCSs leads to more LCS intersections and more uniformly-distributed LCSs entanglements, thus, enhancing fluid exchange throughout the vessel and achieving better mixing. It becomes clear, therefore, that the level of complexity of the uncovered hidden flow structures is directly linked to mixedness. The new Lagrangian approach proposed here, driven by unique PEPT data, has been able to unveil some of the complexities of turbulent flow in a stirred vessel that are beyond the capability of traditional methods and could potentially be exploited for the design of optimal mixing protocols. In addition, by combining the forward and backward FTLE values, a mixing index could be obtained to quantify mixedness in stirred vessels.

CRediT authorship contribution statement

Kun Li: Methodology, Validation, Investigation, Visualization, Writing – original draft. **Chiya Savari:** Methodology, Validation, Visualization, Writing – review & editing. **Mostafa Barigou:** Conceptualization, Methodology, Supervision, Funding acquisition, Writing – review & editing.

Declaration of Competing Interest

The authors declare that they have no known competing financial interests or personal relationships that could have appeared to influence the work reported in this paper.

Acknowledgements

This work was supported by EPSRC Programme Grant EP/R045046/1: Probing Multiscale Complex Multiphase Flows with Positrons for Engineering and Biomedical Applications (PI: Prof. M. Barigou, University of Birmingham).

References

Barigou, M., 2004. Particle Tracking in Opaque Mixing Systems: An Overview of the Capabilities of PET and PEPT. Chem. Eng. Res. Des. 82 (9), 1258–1267.
Barigou, M., Chiti, F., Pianko-Oprych, P., Guida, A., Adams, L., Fan, X., Parker, D.J., Nienow, A.W., 2009. Using Positron Emission Particle Tracking (PEPT) to Study Mixing in Stirred Vessels: Validation and Tackling Unsolved Problems in Opaque Systems. J. Chem. Eng. Jpn. 42 (11), 839–846.
Dauch F., Thilo, Ates, Cihan, Rapp, Tobias, et al., 2019. Analyzing the interaction of vortex and gas-liquid interface dynamics in fuel spray nozzles by means of Lagrangian-coherent structures (2D). Energies 12, (13) 2552. https://doi.org/10.3390/en12132552.
Davidson M, Kyle, Sushil, Shrinivasan, Eggleton D, Charles, Marten R, Mark, 2003. Using computational fluid dynamics software to estimate circulation time distributions in bioreactors. Biotechnol Prog 19, 1480–1486. https://doi.org/10.1021/bp025580d.
D'Ovidio, F., Fernández, V., Hernández-García, E., López, C., 2004. Mixing structures in the Mediterranean Sea from finite-size Lyapunov exponents. Geophys. Res. Lett. 31 (17), n/a–n/a.
Eesa, M., Barigou, M., 2008. Horizontal laminar flow of coarse nearly-neutrally buoyant particles in non-Newtonian conveying fluids: CFD and PEPT experiments compared. Int. J. Multiph. Flow 34 (11), 997–1007.
Fangary, Y.S., Barigou, M., Seville, J.P.K., Parker, D.J., 2002. A Langrangian Study of Solids Suspension in a Stirred Vessel by Positron Emission Particle Tracking (PEPT). Chem. Eng. Technol. 25 (5), 521–528.
Finn, J., Apte, S.V., 2013. Integrated computation of finite-time Lyapunov exponent fields during direct numerical simulation of unsteady flows. Chaos 23 (1), 3500–3524.
Green, M., Rowley, C., Haller, G., 2007. Detection of Lagrangian Coherent Structures in 3D Turbulence. J. Fluid Mech. 572, 111–120.
Guida, A., Nienow, A.W., Barigou, M., 2010a. PEPT measurements of solid-liquid flow field and spatial phase distribution in concentrated monodisperse stirred suspensions. Chem. Eng. Sci. 65 (6), 1905–1914.
Guida, A., Nienow, A. W. & Barigou, M. (2010b), Shannon entropy for local and global description of mixing by Lagrangian particle tracking. Chem. Eng. Sci. 65 (10), 2865–2883.
Guida, A., Nienow, A.W., Barigou, M., 2012. Lagrangian Tools for the Analysis of Mixing in Single-Phase and Multiphase Flow Systems. AIChE Journal 58 (1), 31–45.
Haller, G., Yuan, G., 2000. Lagrangian coherent structures and mixing in two-dimensional turbulence. Physica D 147 (3-4), 352–370.
Haller, G., 2001. Distinguished material surfaces and coherent structures in three-dimensional fluid flows. Physica D 149 (4), 248–277.
Haller, G., 2015. Lagrangian Coherent Structures. Annu. Rev. Fluid Mech. 47 (1), 137–162.
Harnby N., Edwards, M.F., Nienow, A. W., 1997. Mixing in the Process Industries, Butterworth Heinemann.
Hunt, J.C.R., Wray, A.A., Moin, P, 1988. Eddies, stream, and convergence zones in turbulent flows, Center for Turbulence Research, CTR-S88
Jeong, J., Hussain, F., 1995. On the identification of a vortex. J. Fluid Mech. 285, 69–94.
Lekien, F., Coulliette, C., Mariano, A.J., Ryan, E.H., Shay, L.K., Haller, G., Marsden, J., 2005. Pollution release tied to invariant manifolds: A case study for the coast of Florida. Physica D 210 (1-2), 1–20.
Lipinski, D.M., 2012. Efficient ridge tracking algorithms for computing Lagrangian coherent structures in fluid dynamics applications. University of Colorado.
Lukens, S., Yang, X., Fauci, L., 2010. Using Lagrangian coherent structures to analyze fluid mixing by cilia. Chaos 20 (1), 017511. https://doi.org/10.1063/1.3271340.
Olcay, A.B., Pottebaum, T.S., Krueger, P.S., 2010. Sensitivity of Lagrangian coherent structure identification to flow field resolution and random errors. Chaos 20 (1), 017506. https://doi.org/10.1063/1.3276062.
Paul, E.L., Atiemo-Obeng, V.A., Kresta, S.M. (Eds.), 2003. Handbook of Industrial Mixing. John Wiley & Sons, Inc., Hoboken, NJ, USA.
Peng, J., Dabiri, J.O., 2009. Transport of inertial particles by Lagrangian coherent structures: application to predator–prey interaction in jellyfish feeding. J. Fluid Mech. 623, 75–84.
Pianko-Oprych, P., Nienow, A.W., Barigou, M., 2009. Positron Emission Particle Tracking (PEPT) Compared to Particle Image Velocimetry (PIV) for Studying the Flow Generated by a Pitched-Blade Turbine in Single Phase and Multi-Phase Systems. Chem. Eng. Sci. 64 (23), 4955–4968.
Raben, S.G., Ross, S.D., Vlachos, P.P., 2014. Computation of finite-time Lyapunov exponents from time-resolved particle image velocimetry data. Exp. Fluids 55 (1), 1638.
Ricardo, A., Canelas, R., Ferreira, R., 2016. Characterization of vortex interaction with Lagrangian Coherent Structures. In: 8th International Conference on Fluvial Hydraulics, St Louis, pp. 135–141.
Robinso, Martin, Cleary W., Paul, 2011. The influence of cam geometry and operating conditions on chaotic mixing of viscous fluids in a twin cam mixer. AIChE Journal 57 (3), 581–598. https://doi.org/10.1002/aic.1229.
Rom-Kedar, V., Wiggins, S., 1990. Transport in two-dimensional maps. Arch. Ration. Mech. Anal. 109 (3), 239–298.
Ruppert-Felsot, J.E., Praud, O., Sharon, E., Swinney, H.L., 2005. Extraction of coherent structures in a rotating turbulent flow experiment. Phys. Rev. E 72, (2) 016311.
Sapsis, T., Haller, G., 2009. Inertial Particle Dynamics in a Hurricane. J. Atmos. Sci. 66, 2481–2492.
Schindler, B., Peikert, R., Fuchs, R., Theisel, H., 2011. Ridge Concepts for the Visualization of Lagrangian Coherent Structures, Topological Methods in Data Analysis and Visualization II., 221–235. https://doi.org/10.1007/978-3-642-23175-9_15.
Shadden, S.C., Lekien, F., Marsden, J.E., 2005. Definition and properties of Lagrangian coherent structures from finite-time Lyapunov exponents in two-dimensional aperiodic flows. Physica D 212, 271–304.
Shadden, S.C., Taylor, C.A., 2008. Characterization of Coherent Structures in the Cardiovascular System. Ann. Biomed. Eng. 36 (7), 1152–1162.
Shadden, S.C., Lekien, F., Paduan, J.D., Chavez, F.P., Marsden, J.E., 2009. The correlation between surface drifters and coherent structures based on high-frequency radar data in Monterey Bay. Deep Sea Res. Part II 56 (3-5), 161–172.
Shadden, S.C., Astorino, M., Gerbeau, J.-F., 2010. Computational analysis of an aortic valve jet with Lagrangian coherent structures. Chaos: An Interdisciplinary. J. Nonlinear Sci. 20 (1), 017512. https://doi.org/10.1063/1.3272780.
Shadden, S.C., 2011. Lagrangian Coherent Structures. Transport Mixing in Laminar Flows, 59–89.
Sun, P.N., Colagrossi, A., Marrone, S., Zhang, A.M., 2016. Detection of Lagrangian coherent structures in the SPH framework. Comput. Methods Appl. Mech. Eng. 305, 849–868.
Tallapragada, P., Ross, S.D., Schmale, D.G., 2011. Lagrangian coherent structures are associated with fluctuations in airborne microbial populations. Chaos: An Interdisciplinary. J. Nonlinear Sci. 21 (3), 033122. https://doi.org/10.1063/1.3624930.
Tang, J.-N., Tseng, C.-C., Wang, N.-F., 2012. Lagrangian-based investigation of multiphase flows by finite-time Lyapunov exponents. Acta Mech. Sin. 28 (3), 612–624.
Zhou, J., Adrian, R.J., Balachandar, S., Kendall, T.M., 1999. Mechanisms for generating coherent packets of hairpin vortices in channel flow. J. Fluid Mech. 387, 353–396.